Earth's Future

RESEARCH ARTICLE
10.1029/2020EF001942

Key Points:

- Indian Ocean dipole can exert contrasting impacts on gross primary productivity (GPP) over Indian Ocean rim countries driven by precipitation variations
- The recent extremely positive Indian Ocean Dipole (IOD) in 2019 caused the canonical but extreme IOD-affected GPP patterns
- Multimodel future projections suggest that IOD will occur more frequently with larger impacts on GPP, especially over eastern Africa

Supporting Information:

Supporting Information may be found in the online version of this article.

Correspondence to:

J. Wang,
wangjun@nju.edu.cn

Citation:

Wang, J., Wang, M., Kim, J.-S., Joiner, J., Zeng, N., Jiang, F., et al. (2021). Modulation of land photosynthesis by the Indian Ocean Dipole: Satellite-based observations and CMIP6 future projections. *Earth's Future*, *9*, e2020EF001942. https://doi.org/10.1029/2020EF001942

Received 14 DEC 2020
Accepted 30 MAR 2021

Author Contributions:

Conceptualization: Jun Wang, Meirong Wang, Jin-Soo Kim
Data curation: Jun Wang, Meirong Wang
Funding acquisition: Jun Wang, Jin-Soo Kim, Fei Jiang
Investigation: Jun Wang, Jin-Soo Kim
Methodology: Jun Wang
Validation: Jun Wang
Visualization: Jun Wang, Meirong Wang
Writing – original draft: Jun Wang

Modulation of Land Photosynthesis by the Indian Ocean Dipole: Satellite-Based Observations and CMIP6 Future Projections

Jun Wang[1,2], Meirong Wang[3], Jin-Soo Kim[4], Joanna Joiner[5], Ning Zeng[6], Fei Jiang[1,2], Hengmao Wang[1,2], Wei He[1,2], Mousong Wu[1,2], Tiexi Chen[7], Weimin Ju[1,2], and Jing M. Chen[8]

[1]International Institute for Earth System Science, Nanjing University, Nanjing, China, [2]Jiangsu Provincial Key Laboratory of Geographic Information Science and Technology, Key Laboratory for Land Satellite Remote Sensing Applications of Ministry of Natural Resources, School of Geography and Ocean Science, Nanjing University, Nanjing, China, [3]Joint Center for Data Assimilation Research and Applications/Key Laboratory of Meteorological Disaster, Ministry of Education/Joint International Research Laboratory of Climate and Environment Change (ILCEC)/ Collaborative Innovation Center ON Forecast and Evaluation of Meteorological Disasters, Nanjing University of Information Science and Technology, Nanjing, China, [4]Department of Evolutionary Biology and Environmental Studies, University of Zurich, Zurich, Switzerland, [5]Laboratory for Atmospheric Chemistry and Dynamics, National Aeronautics and Space Administration (NASA) Goddard Space Flight Center (GSFC), Greenbelt, MD, USA, [6]Department of Atmospheric and Oceanic Science and Earth System Interdisciplinary Center, University of Maryland, College Park, MD, USA, [7]Collaborative Innovation Center on Forecast and Evaluation of Meteorological Disaster, School of Geographical Sciences, Nanjing University of Information Science & Technology, Nanjing, China, [8]Department of Geography, University of Toronto, Toronto, ON, Canada

Abstract Indian Ocean Dipole (IOD), a major climate variability in the tropics which drives the abiotic stress associated with heavy rainfalls and severe droughts, is not much understood in terms of its role in the carbon cycle, while El Niño-Southern Oscillation (ENSO)-related terrestrial carbon cycle variation has been intensively studied. Here, we investigate IOD's impact on land photosynthesis over the Indian ocean rim countries during austral spring using satellite-based gross primary productivity (GPP) and Earth System Model simulations produced in the Coupled Model Intercomparison Project Phase 6 (CMIP6). IOD independently affects GPP with significant positive partial correlation coefficients (*pcor*) over most of Africa and India, and negative *pcor* over southern China, Indo-China peninsula, maritime continent, and Australia, mostly driven by precipitation variations; this obviously differs from the widespread significant negative *pcor* pattern induced by ENSO. The recent extremely positive IOD in 2019 caused the canonical IOD-affected GPP patterns, however, with its extreme impacts. Furthermore, though large inter-model spreads exist, the CMIP6 multimodel median can basically capture the main characteristics of IOD-affected precipitation and GPP patterns. Importantly, IOD is predicted to occur more frequently in future warming scenarios. Model future projections suggest that it will exert larger impacts on GPP variations over central and eastern Africa, Sumatra, western and southeastern Australia with stronger *pcor* and enhanced explained variance, but less impacts over southern Africa, east India, Indo-China peninsula, and northeastern Australia. Therefore, besides ENSO, understanding the IOD impacts can provide us new insights into regional and global carbon cycle interannual variability.

Plain Language Summary Indian ocean dipole (IOD) is a major climate variability in the tropics, acting as an important determinant of regional climate variations. However, its role in the carbon cycle received less attention. Here we explore the impact of IOD events on land photosynthesis over the Indian ocean rim countries during austral spring based on satellite-based gross primary productivity (GPP) and historical and future simulations in 10 Earth System models. We suggest that IOD can positively impact on GPP over most of Africa and India, but negatively impact over southern China, Indo-China peninsula, maritime continent, and Australia, which are mostly driven by heavy rainfalls and severe droughts associated with its two sea surface temperature poles. The recent extremely positive IOD in 2019 resulted in the canonical but extreme IOD-affected GPP patterns. Furthermore, multimodel future projections suggest that the occurrence of IOD events will be more frequent in future warming scenario. IOD will exert larger impacts on GPP variations over the central and eastern Africa, Sumatra, western and

Writing – review & editing: Jin-Soo Kim, Joanna Joiner, Ning Zeng, Hengmao Wang, Wei He, Mousong Wu, Tiexi Chen, Weimin Ju, Jing M. Chen

southeastern Australia, but lower impacts over southern Africa, east India, the Indo-China peninsula, and northeastern Australia. Understanding the IOD impacts can provide us new insights into regional and global carbon cycle interannual variability.

1. Introduction

Climate variabilities associated with their teleconnections can exert large impacts on terrestrial ecosystems and their carbon cycle. The well-known El Niño-Southern Oscillation (ENSO) dominates the interannual variability of the terrestrial carbon cycle (Bousquet et al., 2000; Kim et al., 2017; Piao et al., 2020; Rodenbeck et al., 2018; Wang, Zeng, Wang, Jiang, Chen, et al., 2018; Zeng et al., 2005), although the dominant climatic driver remains debatable (Ahlstrom et al., 2015; Humphrey et al., 2018; Jung et al., 2017; Wang et al., 2013, 2016; Zeng et al., 2005). The interplay between the North-Atlantic Oscillation (NAO) and East-Atlantic pattern can take the control of the multi-annual variability of European net biome productivity (Bastos et al., 2016). The Pacific Decadal Oscillation and the Atlantic Multidecadal Oscillation are also highly correlated with global and continental carbon fluxes (Zhu et al., 2017).

Indian Ocean Dipole (IOD), the ENSO's neighbor, is an independent air-sea interaction process, acting as an important determinant of regional climate variations on the interannual timescales (Behera et al., 2006; N. H. Saji et al., 1999). Though ENSO and IOD are significantly corelated (N. Saji & Yamagata, 2003), a study (Ham et al., 2016) revealed their weakened coupling in recent decades. Moreover, the frequency of extreme IOD events may increase under the future greenhouse warming (Cai et al., 2014). In the IOD positive phase (denoted as "pIOD"), it shows a pattern with anomalously cool sea surface temperature (SST) off Sumatra and warm SST over the western Indian Ocean during boreal summer and fall, resulting in severe precipitation (floods) in eastern Africa and droughts in Indonesia (Kim et al., 2019; Preethi et al., 2015; N. H. Saji et al., 1999). Further studies suggested that it actually can impact the climate of various parts of the world, especially the Indian Ocean rim countries (Ashok et al., 2004; Cai et al., 2011; Guan et al., 2003; N. Saji & Yamagata, 2003).

However, compared with ENSO events, the impacts of IOD on terrestrial ecosystem and the carbon cycle received less attention. Williams and Hanan (2011) suggested that IOD events can induce large anomalies of photosynthesis across Africa, based on an offline model simulation. They also pointed out that the interference between ENSO and IOD can suppress or even reverse their independent effects. Cai et al. (2009) pointed out that the pIOD event can provide the precondition for the bushfires over the southeast Australia.

More recently, an extreme IOD event occurred in 2019, which was the strongest pIOD in the past two decades. It took large responsibility for the out-of-control mega-bushfires over the eastern Australia in 2019–2020 (Nolan et al., 2020; Phillips & Nogrady, 2020; Wang et al., 2020). Inspired by this extreme event, here we demonstrate the different impacts of IOD and ENSO on terrestrial gross primary productivity (GPP) and investigate the impacts of the recent extreme pIOD, mainly based on climate observations and a newly satellite-based GPP product. Further, we will utilize historical simulations and future projections of 10 Earth System Models (ESM) participating in the Coupled Model Intercomparison Project Phase 6 (CMIP6) (Eyring et al., 2016; C. D. Jones et al., 2016) to investigate the changes of IOD-induced impacts with future greenhouse warming. We expect that this study can give us some new insights into the interannual variability of the terrestrial ecosystem carbon cycle on the global and regional scales.

2. Materials and Methods

2.1. Datasets

Monthly NOAA Optimum Interpolation Sea Surface Temperature (OISST) V2 (Reynolds et al., 2002) was used in this study to illustrate the SST variations with the resolution of $1 \times 1°$. This data set is produced by using in situ and satellite SST observations with the gaps filled in by interpolation.

Global U and V winds at 1,000 and 200 hPa used the Modern-Era Retrospective analysis for Research and Applications, Version 2 (MERRA-2) (Gelaro et al., 2017), which is a NASA atmospheric reanalysis data set utilizing the newer microwave and hyperspectral infrared radiance observations. The MERRA-2 data set

has the horizontal resolution of 0.625 × 0.5° and can be retrieved from the Goddard Earth Sciences Data and Information Services Center (GES DISC).

Land precipitation and surface air temperatures are from the Climatic Research Unit gridded Time Series (CRU TS) v. 4.04 at 0.5° resolution (Harris et al., 2020) which is derived by the interpolation of monthly climate anomalies from weather station observations.

The soil moisture was from the NASA Global Land Data Assimilation System (GLDAS) Noah Land Surface Model L4 monthly V2.1 data set at 0.25° resolution (Rodell et al., 2004). GLDAS-2.1 is forced with a combination of model and observation data including Global Precipitation Climatology Project (Adler et al., 2003) version 1.3 from 2000 to present. The soil moisture in this study refers to the total soil moisture content from surface to the depth of 2 m in the unit of kg m^{-2}.

The global terrestrial GPP is from the FluxSat product version 1 (Joiner et al., 2018) that uses satellite data from the MODerate-resolution Imaging Spectroradiometer (MODIS) within a simplified light-use efficiency (LUE) framework at 0.5° resolution from 2000 to present. It does not depend on other meteorological inputs. Unlike traditional LUE-based model, this data-driven satellite-based GPP product does not use an explicit parameterization of LUE to reduce the value under the limitations such as water and temperature stress. FluxSat performs as well as or better than other state-of-the-art satellite-derived products.

To further verify GPP variations, we additionally used the MODIS MOD13C2 enhanced vegetation index (EVI) in the main text (Didan, 2015) and OCO-2 sun-induced fluorescence (SIF) in the supplementary (Sun et al., 2018). MODIS EVI is a greenness indicator, which conventionally can be used to monitor the terrestrial photosynthetic vegetation activity with good sensitivity over high biomass areas with the original resolution of 0.05°. Satellite observed SIF shows strong relationship with terrestrial GPP (Frankenberg et al., 2011; Guanter et al., 2014). OCO-2 SIF retrievals, starting from September 2014, were aggregated into 2.5 × 2.5° in the supplementary.

2.2. ESM Historical and Future Simulations in CMIP6

We here adopted 10 fully coupled ESM historical simulations and future projections in CMIP6 (Eyring et al., 2016; C. D. Jones et al., 2016) to illustrate the impact of IOD in the future greenhouse warming. In the "esm-hist" simulation which spans the period from 1850 to 2014, ESMs interactively simulated atmospheric CO_2 concentration forced by anthropogenic CO_2 emissions and other prescribed forcing such as non-CO_2 greenhouse gases (GHGs), solar forcing, aerosols, and land cover change. In the "esm-ssp585" simulation which starts from esm-hist simulation and runs up to 2100, ESMs are forced by the emission driven future scenario of Shared Socioeconomic Pathways (SSP)-based Representative Concentration Pathway (RCP) SSP5-8.5.

In detail, the 10 ESMs used here include ACCESS-ESM1.5 (Ziehn et al., 2017), BCC-CSM2-MR (Wu et al., 2019), CanESM5 (Swart et al., 2019), CanESM5-CanOE (Swart et al., 2019), CNRM-ESM2-1 (Séférian et al., 2019), MIROC-ES2L (Hajima et al., 2020), MPI-ESM1.2-LR (Mauritsen et al., 2019), MRI-ESM2-0 (Yukimoto et al., 2019), NorESM2-LM (Seland et al., 2020), and UKESM1-0-LL (Sellar et al., 2019); the information of their land carbon components and horizontal resolutions can be found in Table 1.

In addition, considering the different model horizontal resolutions, we consistently interpolated their simulated variables into 2.5° × 2.5°, based on a first order conservative remapping scheme (P. W. Jones, 1999) via the Climate Data Operators tool which follows the equation:

$$\overline{F_k} = \frac{1}{A_k}\int f dA \tag{1}$$

where $\overline{F_k}$ denotes the area-averaged destination flux, A_k represents the area of grid k, and f is the flux in the original grid cell which has overlapping area A with the destination grid.

Table 1
Fully Coupled Earth System Models (ESM) Used in This Study

Modeling group	ESM	Land carbon/biogeochemistry component	Horizontal resolution	Number of plant functional types
CSIRO	ACCESS-ESM1.5	CABLE2.4 with CASA-CNP	1.875° × 1.25°	13
BCC	BCC-CSM2-MR	BCC-AVIM2	1.125° × 1.125°	16
CCCma	CanESM5-CanOE	CLASS-CTEM	2.81° × 2.81°	9
CCCma	CanESM5	CLASS-CTEM	2.81° × 2.81°	9
CNRM	CNRM-ESM2-1	ISBA-CTRIP	T127	16
JAMSETC	MIROC-ES2L	MATSIRO (physics) VISIT-e (BGC)	2.81° × 2.81°	13
MPI	MPI-ESM1.2-LR	JSBACH3.2	T63	13
MRI	MRI-ESM2-0	HAL1.0	1.125° × 1.12°	10
NCC	NorESM2-LM	CLM5	1.9° × 2.5°	22
UK	UKESM1-0-LL	JULES-ES-1.0	1.875° × 1.25°	13

2.3. Niño 3.4 Index and Dipole Mode Index

We used the Niño 3.4 index to identify the El Niño and La Niña events over the tropical Pacific Ocean. The Niño 3.4 index is defined as the area-averaged SST anomaly over 5°S–5°N, 170°W–120°W relative to the base period from 1981 to 2010. The 3-month running average of Niño 3.4 index is known as Oceanic Niño Index with five consecutive overlapping 3-month periods at or above +0.5° for El Niño and at or below −0.5° for La Niña.

The intensity of IOD is represented by dipole mode index (DMI) (N. H. Saji et al., 1999). The DMI is the anomalous SST gradient between the western equatorial Indian Ocean (10°S–10°N, 50°E–70°E) and the south eastern equatorial Indian Ocean (10°S–0°N, 90°E−110°E). For consistency, the base period is also from 1981 to 2010. We here defined the DMI in SON at or above 1-σ for pIOD and at or below −1-σ for nIOD.

2.4. Velocity Potential and Divergent Winds

In order to better understand the climate anomalies induced by the extreme pIOD in 2019, we here utilized the concept of velocity potential and divergent winds at 200 hPa to infer the vertical motions and divergence of the atmosphere. The relationship between velocity potential (χ) and horizontal velocity vector ($\vec{v}$) is as follows:

$$\nabla^2 \chi = \nabla \cdot \vec{v} \tag{2}$$

We can hence derive the divergent wind components based on the velocity potential as:

$$\left(u_d, v_d\right) = \left(\frac{\partial \chi}{\partial x}, \frac{\partial \chi}{\partial y}\right) \tag{3}$$

where u_d and v_d represent the u and v components of divergent winds.

2.5. Statistical Analysis

In the anomaly calculation for observations, we first removed their long-term climatology, and then detrended them by using a linear regression. The formula of the simple linear regression is as follows:

$$y = \alpha + \beta x + \varepsilon \tag{4}$$

where y is the dependent variable and x is the explanatory variable. α and β denote the y-intercept, and slope, respectively. The term ε denotes the residual error.

For ESM simulated monthly data, considering the nonlinear trends in the long-term periods, we took two steps to get their interannual variability: (1) we made a 12-month running average on raw monthly data to remove the seasonal cycle, (2) we made a 84-month (7-year) running average on raw monthly data to retain their decadal variations and trends. Then the difference between (1) and (2) produces the interannual variability. We then used the anomalies for SON in our analysis.

To broadly understand the impacts of IOD on climate anomalies and GPP, we used partial correlations, as in a previous study (N. Saji & Yamagata, 2003), to investigate its possible impacts excluding the effect of ENSO. The definition of partial correlation coefficient ($pcor$) for x and y, controlling for z follows:

$$pcor_{yx.z} = \frac{r_{yx} - r_{yz}r_{xz}}{\sqrt{1 - r_{yz}^2}\sqrt{1 - r_{xz}^2}} \tag{5}$$

where r_{yx} is the simple correlation of the dependent variable y and the explanatory variable x (say DMI). r_{yz} is the simple correlation of y and z (say Niño 3.4 index), and r_{xz} is the simple correlation of x and z. The statistical significance of the result in each grid is estimated based on the two-tailed Student's t-test:

$$t = pcor_{yx.z}\sqrt{\frac{n - 2 - k}{1 - pcor_{yx.z}^2}} \tag{6}$$

where n represents the number of samples, and k represents the number of variables upon which we are conditioning. Simultaneously, the square of $pcor$, $pcor^2$, explains how much of the variance of y that is not estimated by z is estimated by x.

In CMIP6 ESM simulations, although they are driven by the same prescribed forcing, their simulated internal variabilities (IOD, ENSO etc.) are strongly dependent on each model. Therefore, we first calculated the $pcor$ on each grid for each model and then derive their median $pcor$ to do the analysis here.

Additionally, we also calculated the spatial correlation coefficient ($scor$) to compare their spatial patterns. Owing to higher correlation coefficients among the nearby grids, it is hard to determine the degrees of freedom in space to test the significance for the spatial correlation coefficient. We adopted 1,000 bootstrap estimates (Mudelsee, 2010) to derive the 95% confidence intervals.

3. Results

3.1. Contrasting Impacts of IOD and ENSO on Terrestrial GPP

We here utilized the Niño 3.4 index and DMI to determine the ENSO and IOD events (Figures 1a and 1b). The occurrence of IOD is less frequent than ENSO over the past almost 20 years. The pIOD events basically coincide with El Niño events, and negative IOD (denoted as "nIOD") occur with La Niña events (Figure 1a). However, their correlation coefficient between the DMI during the September–November (SON) and Niño 3.4 index during the December–February (DJF) is 0.37 ($p = 0.13$) for 2001–2019, confirming the result that the ENSO-IOD coupling weakened during the 2000s and 2010s (Ham et al., 2016). The recent extreme pIOD event in 2019 began in the boreal summer, gradually developed, peaked in October with a DMI of 2.3°C, and ended after December (Figure 1b). Concurrently, the Niño 3.4 index indicated a very weak El Niño in 2019, which barely satisfied the criterion (Figure 1b). Considering the limited interference of this very weak El Niño event, this time period presents a good opportunity to investigate the individual influence of the extreme pIOD event on the terrestrial photosynthesis.

In Figure 1c, we examine the SST anomaly averaged from September to November (SON) in 2019 during the extreme pIOD event. This extreme pIOD event is associated with anomalously high SSTs over the western tropical Indian ocean (WTIO) and low SSTs over the southeastern tropical Indian ocean (SETIO) (Figure 1c). Mechanistically, during a pIOD event, SSTs off Sumatra begin to decrease, associated with enhanced southeast trade winds. The enhanced easterly winds along the Equator (Figure 1c) interrupt the normal equatorial current, resulting in the cooling off Sumatra and warm water accumulation over the

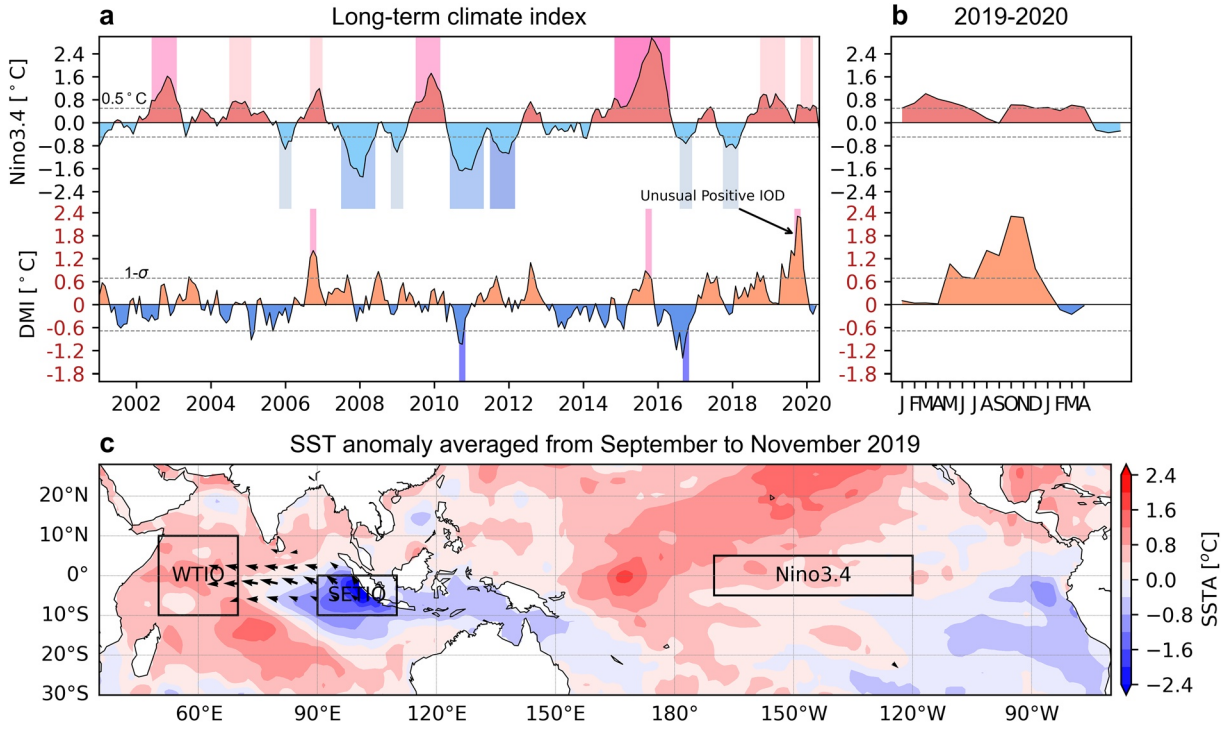

Figure 1. Sea surface temperature anomaly (SSTA). (a) Time series of Niño 3.4 index (top) and dipole mode index (DMI) (bottom). The color bars denote the ENSO and IOD events. And light-to-dark colors in the Niño 3.4 index represent the weak-to-strong ENSO events. (b) Zoom in of the time series from January 2019 to April 2020. (c) Spatial pattern of SSTA averaged from September to November in 2019 with the anomalous winds at 1000 hPa over the tropical Indian Ocean. The black arrows denote the anomalous winds with speeds larger than 2.5 m s^{-1}. The three black boxes show the regions that are used to calculate the Niño 3.4 Index and DMI. ENSO, El Niño-Southern Oscillation; IOD, Indian Ocean Dipole.

WTIO. Moreover, the anomalous trade winds can result in reduced evaporation by enhancing convergence over the WTIO, additionally contributing to warm the SST (N. H. Saji et al., 1999).

Though IOD can influence the climate anomalies over different parts of the world via atmospheric teleconnections (Figure S1), we in this study focused on its impacts over the Indian ocean rim countries during its peak season of SON.

Figures 2a–2c show the *pcor* patterns between climate related or GPP anomalies and Niño 3.4 index, controlling for the effect of DMI. The precipitation shows the significant negative *pcor* with Niño 3.4 index over most of Africa, India, the Indo-China peninsula, maritime continent, and northeast Australia (Figure 2a), whereas temperature basically has the significant positive *pcor* (Figure 2b) owing to the control of thermodynamics and the hydrological cycle (Zeng et al., 2005). These opposing *pcor* distributions indicate widespread warm and dry conditions over the tropics during El Niño events, reducing the terrestrial GPP (Wang et al., 2016; Zeng et al., 2005). Therefore, the *pcor* between GPP and Niño 3.4 index shows significant negative values in general over tropics, especially regions to the north of Lake Victoria over Africa, India, maritime continent, and northeast Australia (Figure 2c), consistent with previous studies (Wang et al., 2016; Zeng et al., 2005). As for the southern China, precipitation has significant positive *pcor* (Figure 2a) and temperature shows a weak negative *pcor* (Figure 2b), resulting in the positive *pcor* between GPP and the Niño 3.4 index (Figure 2c). Over this domain, the *pcor* values for precipitation and GPP show similar probability density distributions, with the positive skewness, while *pcor* values for temperature show negative skewness (Figure 2d).

In contrast, the spatial distributions of *pcor* between climate related or GPP anomalies and DMI, controlling for the effect of the Niño 3.4 index, show obviously different patterns (Figures 2e–2g). Precipitation shows significant positive *pcor* with DMI over most of western, central, and eastern Africa, and India, but significant negative *pcor* over southern China, the maritime continent, and northeast and southeast Australia (Figure 2e). And temperature shows the opposite *pcor* over Africa, southern China, and southeast

10.1029/2020EF001942

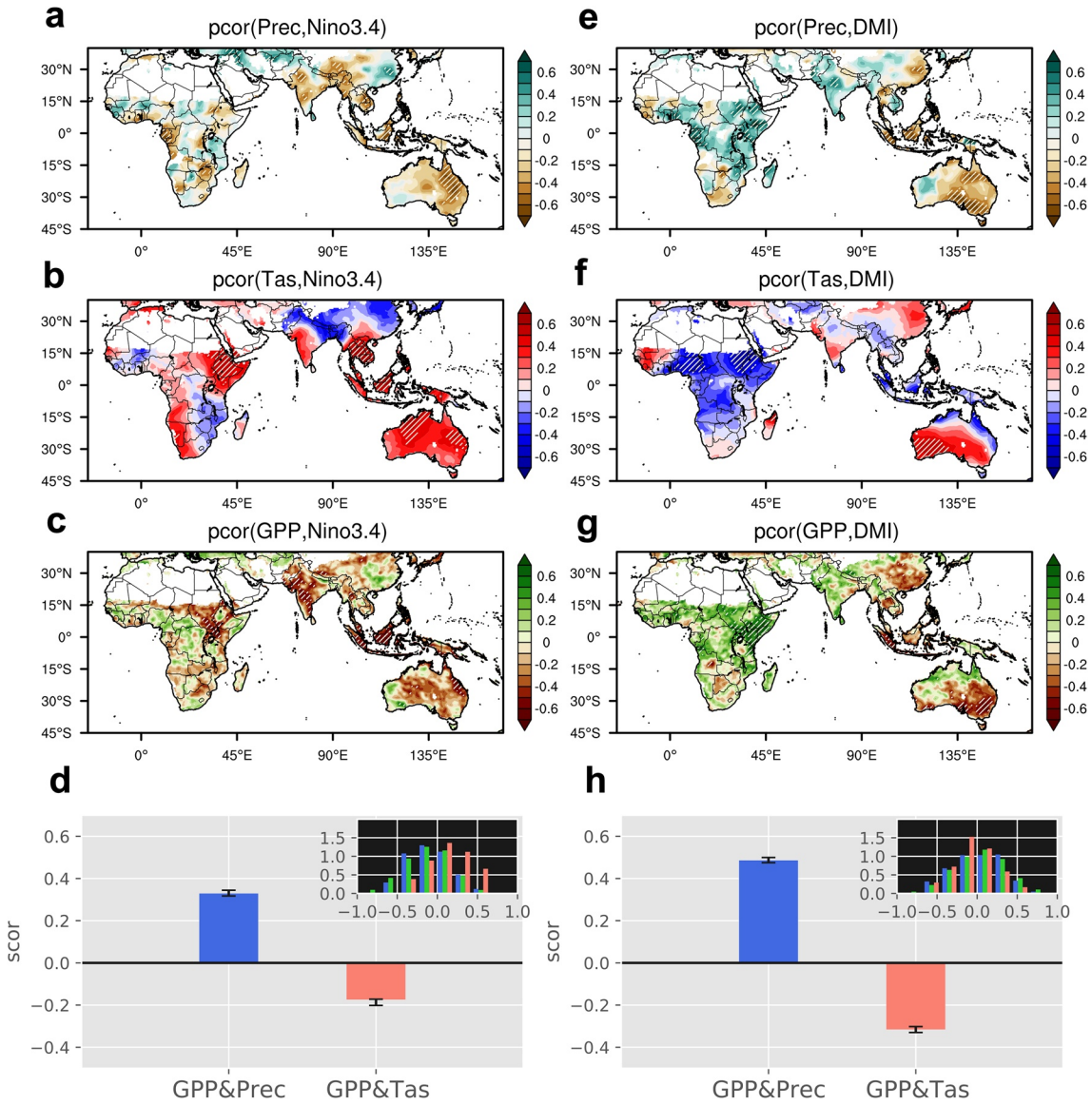

Figure 2. Patterns of partial correlation coefficients (*pcor*). The *pcor* patterns between Niño 3.4 index and precipitation (a), temperature (b), and GPP (c), controlling for the effect of DMI; the *pcor* patterns between DMI and precipitation (e), temperature (f), and GPP (g), controlling for the effect of Niño 3.4 index. The hatched areas represent the significance at $p < 0.05$ based on the two-tailed Student's *t*-test. (d and h) show the spatial correlation coefficients (*scor*) between GPP and climate-related *pcor* patterns with Niño 3.4 index and DMI, respectively. The inserted figures in (d) and (h) represent the probability density distributions for precipitation (light blue), temperature (salmon), and GPP (green) *pcor* with Niño 3.4 index and DMI, respectively. DMI, dipole mode index; GPP, gross primary productivity.

Australia, dominated by thermodynamics and hydrological cycle again (Figure 2f). However, temperature over maritime continent and northeast Australia also shows a negative *pcor*, which could be largely tied to the local SST anomalies (Figures 1c and Fig. 2f). Correspondingly, the *pcor* between GPP and DMI shows the significant positive values over most of western, central, and eastern Africa, and India, while it shows significant negative values over southern China, the Indo-China peninsula, maritime continent, and southeast Australia. The probability density distributions are also almost the same for precipitation and GPP *pcor* values, however, showing negative skewness, while *pcor* values for temperature show positive skewness (Figure 2h).

Additionally, we further calculated their *scor* in Figures 2d and 2h and find that correlation between GPP and precipitation *pcor* patterns has the *scor* = 0.33 for ENSO and 0.49 for IOD, with their 95% confidence

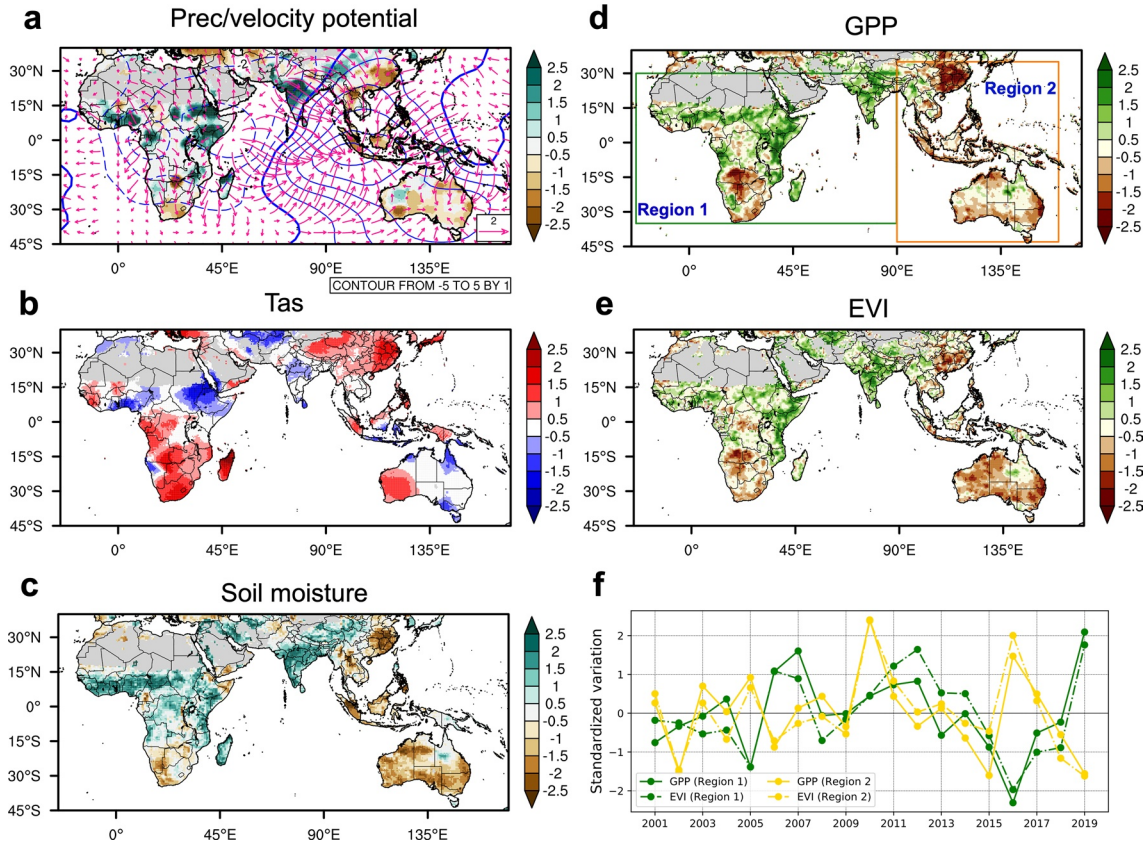

Figure 3. Standardized anomalies during SON in 2019. Climate anomalies for precipitation (a), surface air temperature (b), and soil moisture (c), associated with anomalies of GPP (d) and enhanced vegetation index (EVI) (e). The contour lines and arrows in (a) demonstrate the anomalies of velocity potential and divergent winds at 200 hPa with their respective units of 10^6 m^2 s^{-1} and m s^{-1}. The green and orange boxes in (d) represent two regions of "Region 1" and "Region 2," which are used to calculate the total GPP and area-averaged EVI variations. (f) standardized total GPP and area-averaged EVI time series over Region 1 and Region 2. EVI, enhanced vegetation index; GPP, gross primary productivity.

intervals of [0.32, 0.34] and [0.47, 0.50], respectively. The correlation between GPP and temperature *pcor* patterns produces *scor* = −0.17 for ENSO and −0.32 for IOD, with the 95% confidence intervals of [−0.20, −0.17] and [−0.33, −0.30], respectively. Therefore, the spatial anomalies of GPP during ENSO and IOD events are both more consistent with the patterns of precipitation anomalies than temperature anomalies, implying that precipitation plays a more important role in regional GPP variations, which confirms previous results (Bastos et al., 2018; Wang, Zeng, Wang, Jiang, Wang, & Jiang, 2018).

3.2. Responses to the Recent Extreme pIOD Event in 2019

Figure 3 shows standardized 2019 SON anomalies for climate, GPP, and EVI related to the extreme 2019 pIOD. The warmed SST over WTIO (Figure 1c) resulted in the active convection (Figure 3a), causing more precipitation over western and eastern Africa, western part of central Africa, and India (Figure 3a), associated with lower temperatures (Figure 3b), whereas the cooled SST over SETIO (Figure 1c) was accompanied by subsidence over large areas of ocean and land (Figure 3a), causing less precipitation over southern China, the Indo-China peninsula, maritime continent, and east-central Australia (Figure 3a), associated with higher temperatures except regions largely influenced by local SST anomalies such as northern Australia (Figure 3b). These spatial patterns of precipitation and temperature anomalies resemble their *pcor* distributions calculated with the long-term time series (Figures 2e and 2f), with their *scor* of 0.76 and 0.55 as well as the 95% confidence intervals of [0.76, 0.77] and [0.53, 0.56], respectively. These high *scor* values imply that impacts of the 2019 extreme IOD far outweighed impacts of the concurrent very weak El Niño event. Soil moisture (Figure 3c) is simultaneously affected by precipitation, evaporation, and the soil memory effect.

Its pattern was more consistent with the precipitation anomaly with the *scor* of 0.47 and the 95% confidence interval of [0.45, 0.48].

The wet conditions (Figures 3a and 3c) regulated by warm pole greatly contribute to the enhanced GPP (Figure 3d). Specifically, most of the enhanced GPP over eastern Africa is larger than 2-σ variation. In contrast, the dry conditions (Figures 3a and 3c) regulated by cool pole resulted in the obvious GPP reduction, especially over southern China and eastern Australia with amplitude less than −2-σ variation (Figure 3d). This spatial pattern of anomalous GPP was further confirmed by the MODIS EVI (Figure 3e) and OCO-2 SIF (Figure S2).

According to the contrasting impacts of IOD, we can separate the Indian ocean rim countries into two large regions (denoted as "Region 1" and "Region 2") (Figure 3d). Over Region 1, the variation of total GPP for SON in 2019 shows the strongest positive anomaly from 2001 to 2019, with the departure stronger than 2-σ (Figure 3f). However, over Region 2, the variation of total GPP for SON in 2019 shows one of the strongest negative anomalies, comparable to the reduction induced by extreme El Niño in 2015 (Figure 3f). Also, the EVI variations over these two regions are consistent with GPP variations. These results suggest that the 2019 extreme pIOD event caused extreme GPP anomalies regionally.

3.3. Projected IOD Impacts in Future Greenhouse Warming

We adopted 10 ESMs (Table 1) that participated in CMIP6 to explore the impacts of IOD in the future greenhouse warming, based on two sets of fully coupled simulations, namely "esm-hist" and "esm-ssp585" (C. D. Jones et al., 2016). We here compare the results in 1979–2019 and 2059–2099. Owing to the different strengths of simulated DMI in individual models, we standardized their DMI in SON to show the frequency of IOD occurrences in these two periods (Figure 4a). The multimodel median results suggest that IOD occurrences in 2059–2099 are more frequent than in 1979–2019, albeit a large inter-model spread exists, which is basically consistent with the result, based on CMIP5 multimodel simulations, that greenhouse warming will increase frequency of extreme IOD events (Cai et al., 2014). An increasing frequency of extreme IOD events results from a mean stage change, exerting stronger regulations on climate variabilities over affected regions.

In historical simulations, multimodel median *pcor* between precipitation and DMI, controlling for the effect of the Niño3.4 index, shows significant positive values over the WTIO and eastern Africa, but significant negative values over SETIO, maritime continent and southeast Australia (Figure 4b). Resultantly, the multimodel median *pcor* between GPP and DMI shows significant positive values over eastern Africa, and western part of central Africa, but negative values over southern Africa, India, Indo-China peninsula, maritime continent, and Australia (Figure 4c). These simulated patterns with contrasting influences controlled by two SST poles over the Indian ocean resemble the observations (Figures 2e and 2g), although some differences exist over India with negative *pcor* opposite to the observations, and Sahel and southern China without obvious correlations (Figures 4b and 4c). In individual ESM simulations, though large inter-model differences exist in magnitudes of *pcor* and spatial extent of IOD-related regulations, they basically capture the main characteristics of IOD-affected precipitation (Figure S3) and GPP patterns (Figure S5).

In the future, owing to the increased frequency of IOD occurrences (Figure 4a), multimodel median *pcor* between precipitation and DMI shows the same dipole patterns, but with higher correlations (Figure 4d), associated with higher explained variances over large areas (Figure 4f). Over the Indian ocean rim countries, it is worth mentioning that eastern Africa will experience the most prominent enhancement in *pcor* between precipitation and DMI with the explained variance enhanced by approximately 10% (Figures 4d and 4f). Accordingly, multimodel median *pcor* between GPP and DMI shows the higher positive values over eastern Africa, and lower negative values over Sumatra, western and southeastern Australia (Figure 4e), with the explained variance enhanced by approximately 10% (Figure 4g). This indicates that IOD events will play a more important role in GPP variations over these areas in a future with greenhouse warming. Simultaneously, *pcor* between GPP and DMI over southern Africa, east India, the Indo-China peninsula, and northeastern Australia was weakened (Figure 4e), indicating that IOD event in the future will exert a less important role in GPP variations there with reduced explained variance (Figure 4g). More details for individual model simulations can be found in Figures S4 and S6.

10.1029/2020EF001942

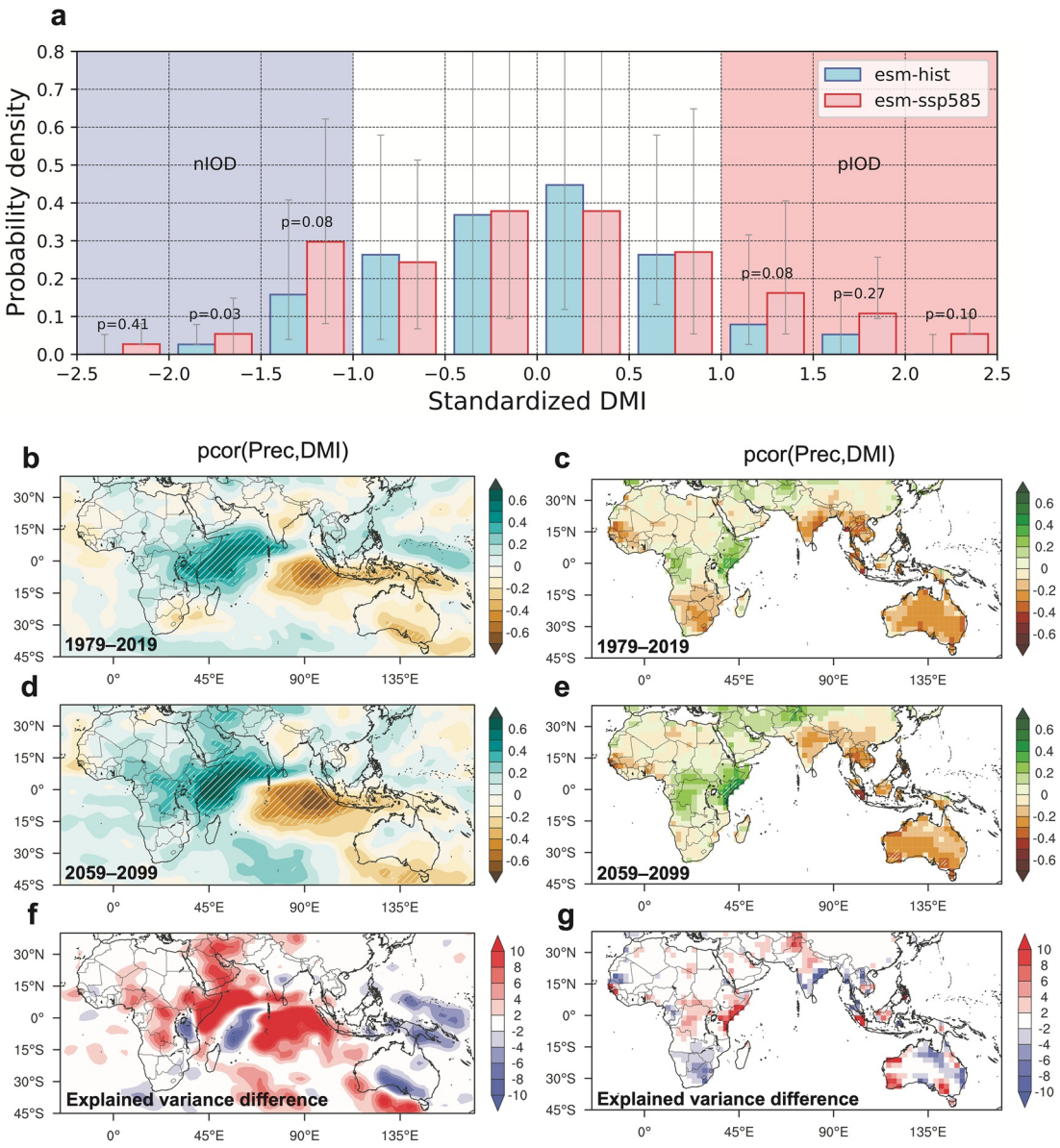

Figure 4. IOD historical and future impacts simulated by fully coupled Earth System Models (ESM) involved in CMIP6. (a) multimodel median probability density distributions of standardized SON DMI during 1979–2019 and 2059–2099. The gray error bars denote the 5% and 95% percentiles in 10 ESM simulations. The p-values are derived from the Wilcoxon rank-sum test. (b) multimodel median *pcor* pattern between precipitation and DMI during 1979–2019, controlling for the effect of the simulated Niño 3.4 index. (c) multimodel median *pr* pattern between GPP and DMI during 1979–2019. (d) multimodel median *pcor* pattern between precipitation and DMI during 2059–2099. (e) multimodel median *pcor* pattern between GPP and DMI during 2059–2099. The hatched areas denote the statistical significance at $p < 0.1$. (f and g) changes of the explained variance for precipitation and GPP in the unit of percentage. DMI, dipole mode index; GPP, gross primary productivity; IOD, Indian Ocean Dipole.

4. Discussion

4.1. Interference Between IOD and ENSO

The IOD event can be triggered by various mechanisms, categorized as the external forcing or internal forcing within the Indian Ocean (Yang et al., 2015), such as the ENSO (Ashok et al., 2003; Guo et al., 2015), Madden Julian Oscillation (Rao et al., 2008), and the Southern Hemisphere Mechanism (SHM) (Zhang et al., 2020). The deep convection will weaken over the maritime continent along with the development of an El Niño event, enhancing the sea level pressure there associated with the anomalous pressure gradient. This enhanced pressure gradient drives easterly wind anomalies over the equatorial Indian Ocean,

replacing the weak climatological westerlies (Meyers et al., 2007). Thus, the El Niño event can trigger a pIOD event, which was regarded as the major external forcing. Therefore, as in Figure 1a, the pIOD events basically occur with El Niño events, and nIOD events occur with La Niña events, with their strong interference. The IOD and ENSO events have the obvious opposite effects on terrestrial GPP variations over most of Africa, India, and Southern China, and same effects over the maritime continent and eastern Australia (Figures 2c and 2g). Therefore, if we only consider the ENSO events, we cannot fully understand these regional GPP variations, as suggested by a previous study (Williams & Hanan, 2011). For a typical example in 2019, a very weak El Niño event occurred. This event obviously cannot explain the warm and severe drought conditions over the eastern Australia, making the devastating bushfires (Boer et al., 2020; Nolan et al., 2020; Wang et al., 2020) and GPP reductions (Figure 3d). Taking both of ENSO and IOD events into account, we can better understand or even predict the variations of these regional ecosystems and carbon cycle.

4.2. Uncertainties in ESM Simulations

Though we suggest that IOD events will exert larger impacts on GPP variations over the central and eastern Africa, Sumatra, western and southeastern Australia, and lower impacts over southern Africa, east India, the Indo-China peninsula, and northeastern Australia, uncertainties remain in our results owing to large inter-model spreads among different ESM simulations (Figures 4a and Figures S3–S6). Figure S7 shows the Taylor diagram for the individual ESM *pcor* pattern against the multimodel median *pcor* pattern calculated from 2059 to 2099. Although they basically capture the main characteristics of IOD-affected GPP patterns (Figure S6), models are quite scattered here (Figure S7). We can clearly see that all but ACCESS-ESM1.5 show higher spatial variations against the multimodel median value. Additionally, the weighted centered pattern correlation coefficients range from 0.22 for MPI-ESM1.2-LR to 0.77 for UKESM1-0-LL, indicating that there are large differences in model simulated *pcor* patterns, which lower the reliability of the multimodel median result. However, McKenna et al. (2020) suggested that the inter-model spread in the frequency of the IOD has reduced in CMIP6 compared to CMIP5. It indicates that continuous developments of ESM can provide us more reliable results for the future projections, providing more opportunities for the further investigation and evaluation.

4.3. Further Work

In this study, we focused on the impact of IOD on terrestrial GPP in its mature phase (SON). The impact of IOD on the terrestrial carbon cycle in its entire life cycle remains unclear. Additionally, it is well known that canonical ENSO events can have lagged effects on the terrestrial carbon cycle, showing that the terrestrial largest carbon flux anomalies lag ENSO events by approximately 4–6 months due to the adjustments of soil moisture and temperature (Qian et al., 2008; Wang et al., 2016; Wang, Zeng, Wang, Jiang, Chen, et al., 2018). Considering the ENSO-IOD coupling, the obvious ENSO lagged effects may have parts of IOD signals. And the study of the lagged effect of IOD is suggested for future research.

5. Conclusion

In this study, we illustrate that IOD events can independently exert large impacts on climate anomalies and terrestrial GPP over the Indian ocean rim countries during its mature season of SON. The partial correlation coefficient (*pcor*) between GPP and DMI shows the significant positive values over western, central, and eastern Africa, and India, and significant negative values over southern China, the Indo-China peninsula, maritime continent, and Australia. This is obviously different from the widespread significant negative *pcor* pattern induced by ENSO events. The recent extreme pIOD event in 2019 caused the canonical IOD-affected GPP patterns with extreme impacts. Total GPP over the "Region 1" has the largest enhancement for the September-November period from 2001 to 2019 with a departure greater than 2-σ variation, while the variation of total GPP over "Region 2" shows one of the strongest reductions, comparable to the amplitude induced by the extreme El Niño in 2015.

Further, we utilized 10 ESM historical simulations and future projections to reveal that the occurrence of IOD events under the future greenhouse warming is very likely more frequent. The multimodel median captures the main characteristics of IOD impacts on precipitation and GPP. Importantly, the median results

suggest that IOD events will exert larger impacts on GPP variations over the central and eastern Africa, Sumatra, western and southeastern Australia with stronger *pcor* and enhanced explained variance (up to approximately 10%), whereas they will play a less important role in GPP variations over southern Africa, east India, the Indo-China peninsula, and northeastern Australia.

Conflict of Interest

The authors declare no competing interests.

Data and Materials Availability

NOAA OISST V2 is provided by the NOAA/OAR/ESRL PSL, Boulder, Colorado, USA, from their web site at https://psl.noaa.gov/. Land precipitation and surface air temperature from CRU TS v. 4.04 are available at https://crudata.uea.ac.uk/cru/data/hrg/. MERRA-2 reanalysis datasets and GLDAS-2.1 are maintained at the NASA Goddard Earth Science Data and Information Services Center (GES DISC) with the web site at https://disc.gsfc.nasa.gov/datasets. Global terrestrial FluxSat GPP can be retrieved at https://avdc.gsfc.nasa.gov/pub/tmp/FluxSat_GPP/. MODIS EVI product can be accessed at https://e4ftl01.cr.usgs.gov/MOLT/MOD13C2.006/. Niño 3.4 index calculated from OISST V2 is available at https://www.cpc.ncep.noaa.gov/data/indices/. CMIP6 multimodel simulation outputs can be freely accessed at https://esgf-node.llnl.gov/projects/cmip6/.

Acknowledgments
We acknowledge the World Climate Research Program, which, through its Working Group on Coupled Modeling, coordinated and promoted CMIP6. We thank the climate modeling groups for producing and making available their model output, the Earth System Grid Federation (ESGF) for archiving the data and providing access, and the multiple funding agencies who support CMIP6 and ESGF. We are grateful to the High Performance Computing Center (HPCC) of Nanjing University for doing the analysis on its blade cluster system. This study was supported by the National Key R&D Program of China (2016YFA0600204) and the National Natural Science Foundation of China (41807434). Jun Wang (201906195014) and Meirong Wang (201908320154) thank the China Scholarship Council for funding. J.-S. Kim was supported by University of Zurich Research Priority Programme "Global Change and Biodiversity" (URPP GCB).

References

Adler, R. F., Huffman, G. J., Chang, A., Ferraro, R., Xie, P.-P., Janowiak, J., et al. (2003). The version-2 global precipitation climatology project (GPCP) monthly precipitation analysis (1979-present). *Journal of Hydrometeorology*, *4*, 1147–1167. https://doi.org/10.1175/1525-7541(2003)004<1147:tvgpcp>2.0.co;2

Ahlstrom, A., Raupach, M. R., Schurgers, G., Smith, B., Arneth, A., Jung, M., et al. (2015). The dominant role of semi-arid ecosystems in the trend and variability of the land CO_2 sink. *Science*, *348*, 895–899. https://doi.org/10.1126/science.aaa1668

Ashok, K., Guan, Z., Saji, N. H., & Yamagata, T. (2004). Individual and combined influences of ENSO and the Indian Ocean Dipole on the Indian summer monsoon. *Journal of Climate*, *17*, 3141–3155. https://doi.org/10.1175/1520-0442(2004)017<3141:iacioe>2.0.co;2

Ashok, K., Guan, Z., & Yamagata, T. (2003). A look at the relationship between the ENSO and the Indian Ocean Dipole. *Journal of the Meteorological Society of Japan*, *81*, 41–56. https://doi.org/10.2151/jmsj.81.41

Bastos, A., Friedlingstein, P., Sitch, S., Chen, C., Mialon, A., Wigneron, J. P., et al. (2018). Impact of the 2015/2016 El Nino on the terrestrial carbon cycle constrained by bottom-up and top-down approaches. *Philosophical Transactions of the Royal Society of London B Biological Sciences*, *373*. https://doi.org/10.1098/rstb.2017.0304

Bastos, A., Janssens, I. A., Gouveia, C. M., Trigo, R. M., Ciais, P., Chevallier, F., et al. (2016). European land CO_2 sink influenced by NAO and East-Atlantic Pattern coupling. *Nature Communications*, *7*, 10315. https://doi.org/10.1038/ncomms10315

Behera, S. K., Luo, J. J., Masson, S., Rao, S. A., Sakuma, H., & Yamagata, T. (2006). A CGCM Study on the Interaction between IOD and ENSO. *Journal of Climate*, *19*, 1688–1705. https://doi.org/10.1175/jcli3797.1

Boer, M. M., Resco de Dios, V., & Bradstock, R. A. (2020). Unprecedented burn area of Australian mega forest fires. *Nature Climate Change*, *10*, 171–172. https://doi.org/10.1038/s41558-020-0716-1

Bousquet, P., Peylin, P., Ciais, P., Le Quere, C., Friedlingstein, P., & Tans, P. P. (2000). Regional changes in carbon dioxide fluxes of land and oceans since 1980. *Science*, *290*, 1342–1346. https://doi.org/10.1126/science.290.5495.1342

Cai, W., Cowan, T., & Raupach, M. (2009). Positive Indian Ocean Dipole events precondition southeast Australia bushfires. *Geophysical Research Letters*, *36*. https://doi.org/10.1029/2009gl039902

Cai, W., Santoso, A., Wang, G., Weller, E., Wu, L., Ashok, K., et al. (2014). Increased frequency of extreme Indian Ocean Dipole events due to greenhouse warming. *Nature*, *510*, 254–258. https://doi.org/10.1038/nature13327

Cai, W., van Rensch, P., Cowan, T., & Hendon, H. H. (2011). Teleconnection pathways of ENSO and the IOD and the mechanisms for impacts on Australian rainfall. *Journal of Climate*, *24*, 3910–3923. https://doi.org/10.1175/2011jcli4129.1

Didan, K. (2015). *MOD13C2 MODIS/Terra vegetation indices monthly L3 Global 0.05Deg CMG V006*. NASA EOSDIS Land Processes DAAC.

Eyring, V., Bony, S., Meehl, G. A., Senior, C. A., Stevens, B., Stouffer, R. J., & Taylor, K. E. (2016). Overview of the Coupled Model Intercomparison Project Phase 6 (CMIP6) experimental design and organization. *Geoscientific Model Development*, *9*, 1937–1958. https://doi.org/10.5194/gmd-9-1937-2016

Frankenberg, C., Fisher, J. B., Worden, J., Badgley, G., Saatchi, S. S., Lee, J. E., et al. (2011). New global observations of the terrestrial carbon cycle from GOSAT: Patterns of plant fluorescence with gross primary productivity. *Geophysical Research Letters*, *38*, L17706. https://doi.org/10.1029/2011gl048738

Gelaro, R., McCarty, W., Suárez, M. J., Todling, R., Molod, A., Takacs, L., et al. (2017). The Modern-Era Retrospective Analysis for Research and Applications, Version 2 (MERRA-2). *Journal of Climate*, *30*, 5419–5454. https://doi.org/10.1175/jcli-d-16-0758.1

Guan, Z., Ashok, K., & Yamagata, T. (2003). Summertime response of the tropical atmosphere to the Indian ocean dipole sea surface temperature anomalies. *Journal of the Meteorological Society of Japan*, *81*, 533–561. https://doi.org/10.2151/jmsj.81.533

Guanter, L., Zhang, Y., Jung, M., Joiner, J., Voigt, M., Berry, J. A., et al. (2014). Global and time-resolved monitoring of crop photosynthesis with chlorophyll fluorescence. *Proceedings of the National Academy of Sciences*, *111*, E1327–E1333. https://doi.org/10.1073/pnas.1320008111

Guo, F., Liu, Q., Sun, S., & Yang, J. (2015). Three types of Indian Ocean Dipoles. *Journal of Climate*, *28*, 3073–3092. https://doi.org/10.1175/jcli-d-14-00507.1

Hajima, T., Watanabe, M., Yamamoto, A., Tatebe, H., Noguchi, M. A., Abe, M., et al. (2020). Development of the MIROC-ES2L Earth system model and the evaluation of biogeochemical processes and feedbacks. *Geoscientific Model Development*, *13*, 2197–2244. https://doi.org/10.5194/gmd-13-2197-2020

Ham, Y.-G., Choi, J.-Y., & Kug, J.-S. (2016). The weakening of the ENSO-Indian Ocean Dipole (IOD) coupling strength in recent decades. *Climate Dynamics*, *49*, 249–261. https://doi.org/10.1007/s00382-016-3339-5

Harris, I., Osborn, T. J., Jones, P., & Lister, D. (2020). Version 4 of the CRU TS monthly high-resolution gridded multivariate climate dataset. *Scientific Data*, *7*, 109. https://doi.org/10.1038/s41597-020-0453-3

Humphrey, V., Zscheischler, J., Ciais, P., Gudmundsson, L., Sitch, S., & Seneviratne, S. I. (2018). Sensitivity of atmospheric CO_2 growth rate to observed changes in terrestrial water storage. *Nature*, *560*, 628.-+ https://doi.org/10.1038/s41586-018-0424-4

Joiner, J., Yoshida, Y., Zhang, Y., Duveiller, G., Jung, M., Lyapustin, A., et al. (2018). Estimation of terrestrial global gross primary production (GPP) with satellite data-driven models and eddy covariance flux data. *Remote Sensing*, *10*. https://doi.org/10.3390/rs10091346

Jones, C. D., Arora, V., Friedlingstein, P., Bopp, L., Brovkin, V., Dunne, J., et al. (2016). C4MIP—The coupled climate-carbon cycle model intercomparison project: Experimental protocol for CMIP6. *Geoscientific Model Development*, *9*, 2853–2880. https://doi.org/10.5194/gmd-9-2853-2016

Jones, P. W. (1999). First- and second-order conservative remapping schemes for grids in spherical coordinates. *Monthly Weather Review*, *127*, 2204–2210. https://doi.org/10.1175/1520-0493(1999)127<2204:fasocr>2.0.co;2

Jung, M., Reichstein, M., Schwalm, C. R., Huntingford, C., Sitch, S., Ahlström, A., et al. (2017). Compensatory water effects link yearly global land CO_2 sink changes to temperature. *Nature*, *541*, 516–520. https://doi.org/10.1038/nature20780

Kim, J. S., Jeong, S. J., Kug, J. S., & Williams, M. (2019). Role of local air-sea interaction in fire activity over equatorial Asia. *Geophysical Research Letters*, *46*, 14789–14797. https://doi.org/10.1029/2019gl085943

Kim, J.-S., Kug, J.-S., & Jeong, S.-J. (2017). Intensification of terrestrial carbon cycle related to El Niño–Southern Oscillation under greenhouse warming. *Nature Communications*, *8*. https://doi.org/10.1038/s41467-017-01831-7

Mauritsen, T., Bader, J., Becker, T., Behrens, J., Bittner, M., Brokopf, R., et al. (2019). Developments in the MPI-M Earth System Model version 1.2 (MPI-ESM1.2) and its response to increasing CO_2. *Journal of Advances in Modeling Earth Systems*, *11*, 998–1038. https://doi.org/10.1029/2018ms001400

McKenna, S., Santoso, A., Gupta, A. S., Taschetto, A. S., & Cai, W. (2020). Indian Ocean Dipole in CMIP5 and CMIP6: Characteristics, biases, and links to ENSO. *Scientific Reports*, *10*, 11500. https://doi.org/10.1038/s41598-020-68268-9

Meyers, G., McIntosh, P., Pigot, L., & Pook, M. (2007). The years of El Niño, La Niña, and Interactions with the Tropical Indian Ocean. *Journal of Climate*, *20*, 2872–2880. https://doi.org/10.1175/jcli4152.1

Mudelsee, M. (2010). *Climate time series analysis: Classical statistical and bootstrap methods* (1st ed.). Springer.

Nolan, R. H., Boer, M. M., Collins, L., Resco de Dios, V., Clarke, H., Jenkins, M., et al. (2020). Causes and consequences of eastern Australia's 2019-20 season of mega-fires. *Global Change Biology*, *26*, 1039–1041. https://doi.org/10.1111/gcb.14987

Phillips, N., & Nogrady, B. (2020). The race to decipher how climate change influenced Australia's record fires. *Nature*, *577*, 610–612. https://doi.org/10.1038/d41586-020-00173-7

Piao, S., Wang, X., Wang, K., Li, X., Bastos, A., Canadell, J. G., et al. (2020). Interannual variation of terrestrial carbon cycle: Issues and perspectives. *Global Change Biology*, *26*, 300–318. https://doi.org/10.1111/gcb.14884

Preethi, B., Sabin, T. P., Adedoyin, J. A., & Ashok, K. (2015). Impacts of the ENSO Modoki and other Tropical Indo-Pacific Climate-Drivers on African Rainfall. *Scientific Reports*, *5*, 16653. https://doi.org/10.1038/srep16653

Qian, H., Joseph, R., & Zeng, N. (2008). Response of the terrestrial carbon cycle to the El Ni˜no-Southern Oscillation. *Tellus B: Chemical and Physical Meteorology*, *60*, 537–550. https://doi.org/10.1111/j.1600-0889.2008.00360.x

Rao, S. A., Luo, J.-J., Behera, S. K., & Yamagata, T. (2008). Generation and termination of Indian Ocean dipole events in 2003, 2006 and 2007. *Climate Dynamics*, *33*, 751–767. https://doi.org/10.1007/s00382-008-0498-z

Reynolds, R. W., Rayner, N. A., Smith, T. M., Stokes, D. C., & Wang, W. (2002). An Improved In Situ and Satellite SST Analysis for Climate. *Journal of Climate*, *15*, 1609–1625. https://doi.org/10.1175/1520-0442(2002)015<1609:aiisas>2.0.co;2

Rodell, M., Houser, P. R., Jambor, U., Gottschalck, J., Mitchell, K., Meng, C.-J., et al. (2004). The global land data assimilation system. *Bulletin of the American Meteorological Society*, *85*, 381–394. https://doi.org/10.1175/bams-85-3-381

Rodenbeck, C., Zaehle, S., Keeling, R., & Heimann, M. (2018). History of El Nino impacts on the global carbon cycle 1957-2017: A quantification from atmospheric CO_2 data. *Philosophical Transactions of the Royal Society of London B Biological Sciences*, *373*. https://doi.org/10.1098/rstb.2017.0303

Saji, N., & Yamagata, T. (2003). Possible impacts of Indian Ocean Dipole mode events on global climate. *Climate Research*, *25*, 151–169. https://doi.org/10.3354/cr025151

Saji, N. H., Goswami, B. N., Vinayachandran, P. N., & Yamagata, T. (1999). A dipole mode in the tropical Indian Ocean. *Nature*, *401*, 360–363. https://doi.org/10.1038/43854

Séférian, R., Nabat, P., Michou, M., Saint-Martin, D., Voldoire, A., Colin, J., et al. (2019). Evaluation of CNRM Earth System Model, CNRM-ESM2-1: Role of Earth system processes in present-day and future climate. *Journal of Advances in Modeling Earth Systems*, *11*, 4182–4227. https://doi.org/10.1029/2019ms001791

Seland, Ø., Bentsen, M., Seland Graff, L., Olivié, D., Toniazzo, T., Gjermundsen, A., et al. (2020). The Norwegian Earth System Model, NorESM2—Evaluation of the CMIP6 DECK and historical simulations. *Geoscientific Model Development Discussion*.

Sellar, A. A., Jones, C. G., Mulcahy, J. P., Tang, Y., Yool, A., Wiltshire, A., et al. (2019). UKESM1: Description and evaluation of the U.K. Earth System Model. *Journal of Advances in Modeling Earth Systems*, *11*, 4513–4558. https://doi.org/10.1029/2019ms001739

Sun, Y., Frankenberg, C., Jung, M., Joiner, J., Guanter, L., Köhler, P., & Magney, T. (2018). Overview of solar-induced chlorophyll fluorescence (SIF) from the Orbiting Carbon Observatory-2: Retrieval, cross-mission comparison, and global monitoring for GPP. *Remote Sensing of Environment*, *209*, 808–823. https://doi.org/10.1016/j.rse.2018.02.016

Swart, N. C., Cole, J. N. S., Kharin, V. V., Lazare, M., Scinocca, J. F., Gillett, N. P., et al. (2019). The Canadian Earth System Model version 5 (CanESM5.0.3). *Geoscientific Model Development*, *12*, 4823–4873. https://doi.org/10.5194/gmd-12-4823-2019

Wang, J., Liu, Z., Zeng, N., Jiang, F., Wang, H., & Ju, W. (2020). Spaceborne detection of XCO_2 enhancement induced by Australian mega-bushfires. *Environmental Research Letters*, *15*, 124069. https://doi.org/10.1088/1748-9326/abc846

Wang, J., Zeng, N., & Wang, M. (2016). Interannual variability of the atmospheric CO_2 growth rate: Roles of precipitation and temperature. *Biogeosciences*, *13*, 2339–2352. https://doi.org/10.5194/bg-13-2339-2016

Wang, J., Zeng, N., Wang, M., Jiang, F., Chen, J., Friedlingstein, P., et al. (2018). Contrasting interannual atmospheric CO_2 variabilities and their terrestrial mechanisms for two types of El Niños. *Atmospheric Chemistry and Physics*, *18*, 10333–10345. https://doi.org/10.5194/acp-18-10333-2018

Wang, J., Zeng, N., Wang, M., Jiang, F., Wang, H., & Jiang, Z. (2018). Contrasting terrestrial carbon cycle responses to the 1997/98 and 2015/16 extreme El Niño events. *Earth System Dynamics*, *9*, 1–14. https://doi.org/10.5194/esd-9-1-2018

Wang, W., Ciais, P., Nemani, R. R., Canadell, J. G., Piao, S., Sitch, S., et al. (2013). Variations in atmospheric CO_2 growth rates coupled with tropical temperature. *Proceedings of the National Academy of Sciences*, *110*, 13061–13066. https://doi.org/10.1073/pnas.1219683110

Williams, C. A., & Hanan, N. P. (2011). ENSO and IOD teleconnections for African ecosystems: Evidence of destructive interference between climate oscillations. *Biogeosciences*, *8*, 27–40. https://doi.org/10.5194/bg-8-27-2011

Wu, T., Lu, Y., Fang, Y., Xin, X., Li, L., Li, W., et al. (2019). The Beijing Climate Center Climate System Model (BCC-CSM): The main progress from CMIP5 to CMIP6. *Geoscientific Model Development*, *12*, 1573–1600. https://doi.org/10.5194/gmd-12-1573-2019

Yang, Y., Xie, S.-P., Wu, L., Kosaka, Y., Lau, N.-C., & Vecchi, G. A. (2015). Seasonality and predictability of the Indian Ocean Dipole Mode: ENSO forcing and internal variability. *Journal of Climate*, *28*, 8021–8036. https://doi.org/10.1175/jcli-d-15-0078.1

Yukimoto, S., Kawai, H., Koshiro, T., Oshima, N., Yoshida, K., Urakawa, S., et al. (2019). The Meteorological Research Institute Earth System Model Version 2.0, MRI-ESM2.0: Description and basic evaluation of the physical component. *Journal of the Meteorological Society of Japan*, *97*, 931–965. https://doi.org/10.2151/jmsj.2019-051

Zeng, N., Mariotti, A., & Wetzel, P. (2005). Terrestrial mechanisms of interannual CO_2 variability. *Global Biogeochemical Cycles*, *19*, GB1016. https://doi.org/10.1029/2004gb002273

Zhang, L. Y., Du, Y., Cai, W., Chen, Z., Tozuka, T., & Yu, J. Y. (2020). Triggering the Indian Ocean Dipole from the Southern Hemisphere. *Geophysical Research Letters*, *47*. https://doi.org/10.1029/2020gl088648

Zhu, Z., Piao, S., Xu, Y., Bastos, A., Ciais, P., & Peng, S. (2017). The effects of teleconnections on carbon fluxes of global terrestrial ecosystems. *Geophysical Research Letters*, *44*, 3209–3218. https://doi.org/10.1002/2016gl071743

Ziehn, T., Lenton, A., Law, R. M., Matear, R. J., & Chamberlain, M. A. (2017). The carbon cycle in the Australian Community Climate and Earth System Simulator (ACCESS-ESM1)—Part 2: Historical simulations. *Geoscientific Model Development*, *10*, 2591–2614. https://doi.org/10.5194/gmd-10-2591-2017